Nano Energy 50 (2018) 245–255

Contents lists available at ScienceDirect

Nano Energy

journal homepage: www.elsevier.com/locate/nanoen

Full paper

Type-I alignment in $MAPbI_3$ based solar devices with doped-silicon nanocrystals

Conor Rocks[a,*], Vladimir Svrcek[b], Tamilselvan Velusamy[a], Manuel Macias-Montero[a], Paul Maguire[a], Davide Mariotti[a]

[a] Nanotechnology & Integrated Bio-Engineering Centre (NIBEC), Ulster University, UK
[b] Research Center for Photovoltaics, National Institute of Advanced Industrial Science and Technology (AIST), Central 2, Umezono 1-1-1, Tsukuba 305-8568, Japan

ARTICLE INFO

Keywords:
Perovskite
Silicon nanocrystals
Quantum dots
Solar cells
Type-I alignment

ABSTRACT

In this work we couple silicon nanocrystals (Si NCs) with strong quantum confinement (< 4 nm diameter) with large grained $MAPbI_3$ films combining the perovskites excellent transport properties with the unique opto-electronic properties of quantum confined Si NCs. The electronic structures of $MAPbI_3$ and Si NCs, ideally aligned to form a type-I heterojunction, demonstrated improved carrier collection through a higher short-circuit current density (~ 20 mA cm^{-2}) measured in photovoltaic test devices. The addition of p- and n-doped Si NCs within the $MAPbI_3$ films also showed unexpected and interesting device performance improvements, where the typical perovskite degradation process in ambient conditions was considerably slowed down and the overall device efficiency was observed to increase under light soaking. We attribute these improvements to the presence of Si NCs, which helped maintain the perovskite film qualities for more than 14 days in open atmosphere.

1. Introduction

Organic-inorganic halide perovskites have received great interest in opto-electronic applications due to their high absorption of light, increased diffusion lengths and low exciton binding energies and were therefore successfully exploited for high efficiency solar devices [1–3]. These perovskites contain a small organic cation ($CH_3NH_3^+$) at the core which is surrounded by octahedral network made up of a metal cation (Pb^{2+}) and a monovalent halide anion (I^-). Despite the large rise in efficiency of perovskite devices, a number of problems concerning the operation and stability are a major factor in the feasibility of large scale roll out. The hysteresis phenomena commonly observed has been related to a number of internal mechanisms that act concurrently such as trapping of charge carriers, [4] reorientation of ferroelectric organic cations, [5] polarization and ion migration [6,7]. Additionally exposure to atmospheric conditions and highly humid environments are detrimental to perovskites chemical stability. Methylammonium lead iodide ($MAPbI_3$), despite displaying the most favourable properties, also displays the most rapid chemical degradation which can occur through a number of pathways. The initial step in the degradation process is understood to be the deprotonation of MA cation that stems from weak hydrogen bonding with the PbI_6 network [8,9]. The PbI_6 octahedral is rearranged due to the loss of I atoms to MAI and HI components that allows for a PbI_2 crystal seed to form [10]. The breakdown of the perovskite structure and consequently their enhanced opto-electronic properties is a limiting factor for use in long term solar cells applications.

Quantum dots (QDs) have suffered and slowed in their development for solar cell applications as a direct consequence of the recent perovskite trend. Their unique opto-electronic properties based on quantum confinement effects make them ideal for a range of applications such as bio-imaging, drug delivery, LEDs as well as solar cells [11–13]. Quantum confinement effects (QCEs) generally lead to a widening of the material bandgap that allows tuning of bandgap energy as a function of particle size [14]. Another QCE is the increase in oscillator strength that is expected to result in higher absorption coefficients and for instance impact at a larger extent the indirect bandgap of materials such as Si [15,16]. Because of the dominance that Si has shown in the opto-electronic industry over recent decades, silicon QDs, or nanocrystals (Si NCs), and their associated properties are of great interest. One of the most exciting phenomena that has been demonstrated in Si NCs is carrier multiplication (CM), which has the possibility of increasing the theoretical limit of photovoltaic cells up to 42% [17,18]. Coupling of different materials can produce interesting composites that may lead to new properties and interesting synergies. While bulk silicon-$MAPbI_3$ planar junctions have been reported, [19] the use of quantum confined Si NCs in the $MAPbI_3$ matrix has not been investigated; in comparison to bulk silicon, in addition to offering the

* Corresponding author.
E-mail address: rocks-c2@ulster.ac.uk (C. Rocks).

https://doi.org/10.1016/j.nanoen.2018.05.036
Received 27 March 2018; Accepted 16 May 2018
Available online 18 May 2018

opportunity for complete new device architectures, the properties of Si NCs also make available new mechanisms for carrier generation and dissociation. The potential interactions between the complex perovskite structure and small size Si NCs could allow for new phenomena, where recently an exciplet state was observed between PbS QDs and perovskite films that are promising for intermediate band gap solar cells [20].

In this work, efforts were made to mix both p-doped (p-) and n-doped (n-) Si NCs in $MAPbI_3$ films at a small weight ratio (10:90). The motivation for studying this composite perovskite-Si NCs films was the atypical band alignment forming a type-I heterojunction, which has not been predominantly utilized and is believed to represent a novel approach to the wider family of QD solar cell device architectures. A type-I alignment leads to the possibility of enhanced carrier extraction and in general synergies between the respective materials qualities (e.g. carrier multiplication for Si NCs and exceptional transport for perovskites). Our work has also revealed additional advantages (i.e. moisture resistance and stability) where our devices made of perovskite/Si NCs composites also presented better resistance to moisture and improved stability compared to the perovskite-only devices.

We report a detailed materials characterization of the composite films and we have studied the films properties through test photovoltaic device structures. The electronic band structure for doped Si NCs and $MAPbI_3$ was experimentally determined using a combination of techniques revealing type-I band alignment. Detailed chemical analysis performed for composite $MAPbI_3$/QD films highlighted changes in surface chemistry that improves $MAPbI_3$ film stability in ambient conditions. The photovoltaic performance of test structures with $MAPbI_3$ films and composite $MAPbI_3$ + doped Si NC films were measured under light soaking conditions (0–8 min) to determine changes in light response over time. Subsequently, JV measurements are taken after 7 and 14 days in ambient atmosphere to determine effects of aging and highlight the complementary role that Si NCs play in creating more stable devices.

2. Experimental section

2.1. Synthesis and characterization of Si nanocrystals, $MAPbI_3$ films and composite films

Boron-doped silicon wafers (0.1 Ω cm, 0.5 mm thickness) and phosphorous-doped silicon wafers (0.1–0.5 Ω cm, 0.5 mm thickness) were used during an electrochemical etching process to synthesise p-type and n-type Si NCs. Both p- and n-Si NCs synthesized with this method and used in this work have been characterized extensively by our group where a typical size distribution is < 10 nm and show strong quantum confinement [21–23]. Representative transmission electron microscopy (TEM) images along with particle size distributions are presented in the Supporting information. TEM analysis was done using a JEOL 2100-F electron microscope at an acceleration voltage of 200 kV. Both p- and n-Si NCs where drop casted from colloidal solution following an ultra-sonication process and tranferred onto a carbon holey grid. Log normal fits of the distribution gave the mean particle diameter equal to 1.79 ± 0.88 nm for p-Si NCs and 2.76 ± 1.72 nm for n-Si NCs. High resolution image of single p- and n-Si NCs highlight clear lattice fringes that confirm the crystalline nature of the particles. Methylammonium lead iodide ($CH_3NH_3PbI_3$) perovskite powder with 99% purity was purchased from Xi'an polymer light technology. Scanning electron microscopy (SEM) was used to image the surface of $MAPbI_3$ films that were deposited using a one-step spray technique (see Supporting information). SEM was performed using a JEOL JSM-6010PLUS at 20 kV acceleration voltages. Composite films incorporating perovskite + p-type Si NCs and perovskite + n-type Si NCs were fabricated by mixing with aforementioned perovskite solution at 10% weight percentage (90:10). Prior to mixing both p- and n-type Si NCs underwent an ultra-sonication process to assist in the fragmentation of agglomerates. X-ray diffraction (XRD) analysis (see Supporting information) showed no differences in the corresponding diffraction peaks for the $MAPbI_3$ films with/without Si NCs. The average crystallite size was determined using the Scherrer's formula, with the pristine $MAPbI_3$ film giving sizes of 58.21 ± 8.32 nm versus 54.96 ± 5.07 nm for the composite film with p-Si NCs included. A Bruker D8 diffractometer was used for XRD analysis. X-ray photoelectron spectroscopy (XPS) to determine surface chemical composition of the films was performed using an X-ray source Al = 1486 eV) and the Kratos AxisUltra DLD spectrometer with peak fitting performed using Kratos software. Current and voltage were 10 mA and 15 kV respectively with an operating pressure of 10^{-9} bar. Specific region scans were performed at a resolution of 0.05 eV and pass energy of 20 eV. X-ray spot size and hence capture area is equal to 400 μm^2 with a penetration depth of 10 nm. XPS spectra were calibrated to 284.8 eV according to the C *1s* binding energy for adventitious carbon.

2.2. Solar cell fabrication and characterization

Glass substrates were purchased from VisionTek which included patterned strips of indium-doped tin oxide (ITO, 150 nm thick, 15 Ω/sq and 2 mm wide). Triethanolamine, titanium isopropoxide purchased from Sigma-Aldrich were used for fabrication of compact TiO_2 blocking layer in solar cell devices. Solution of TiO_2 was created using a mixture of triethanolamine (0.39 g) and Titanium (IV) isopropoxide (1.56 mL) with ethanol (18 mL) before mixing at 40 °C for 2 h then left overnight. The solution was then spin coated at 5000 rpm for 30 s on top of the ITO coated glass substrate followed by annealing the film at 400 °C for 3 h. Sigma-Aldrich purchased Titanium oxide anatase nanopowder (< 25 nm diameter), was used in the fabrication of a porous layer in the solar cell devices. A solution of 40 mg Titanium (IV) oxide anatase nanopowder and 20 mL of ethanol/DI-water (1:1) was mixed and sonicated for 30 min followed by an additional settling period of 30 min. 400 μL were then sprayed using an airbrush (pro series BD-132) in open atmosphere via nitrogen gas flow at 1 bar pressure positioned 15 cm above a hot plate at 0° angle incident to substrate surface. This method of deposition was first demonstrated in a previous publication by the group [24]. Following deposition, the film is annealed for 1 h at 150 °C to form the meso-porous TiO_2 layer. Methylammonium lead iodide ($CH_3NH_3PbI_3$) perovskite powder with/without Si NCs as previously described is mixed in dimethylformamide (DMF) at 60 °C at 0.125 M (1 M = 0.619.9 g/mL) and sprayed using the same set up. The film is then annealed for 40 min at 100 °C. Finally, for use in photovoltaic device, gold (Au) contacts are deposited using a Moorfield minlab DC/RF magnetron box sputter system using argon plasma at constant current of 0.15 A for 60 min with a working pressure of 1.5×10^{-2} mbar. Current density-voltage (JV) curves of devices incorporating sprayed $MAPbI_3$ films were recorded by a Keithley 6430 sub-FA sourcemeter unit under illumination 1.5 AM in air at ambient temperature. The applied bias varied from − 1 V to1 V in steps of 0.01 V at a scan rate 700 mV s^{-1} consistently for all devices.

2.3. Energy band diagram measurements

The Fermi level measurements were characterized using a scanning Kelvin probe system (KPTechnology) across an area on the samples surface and presented as a 3D map. Ultraviolet-visible (UV–Vis) absorption measurements are carried out using a deuterium-halogen light source and an integrating sphere. XPS was also used to determine the valence band edges of the materials.

3. Results and discussion

3.1. Chemical analysis and stability of $MAPbI_3$ + p- and n-Si NC Films

We first analyse the chemical properties of the composite films

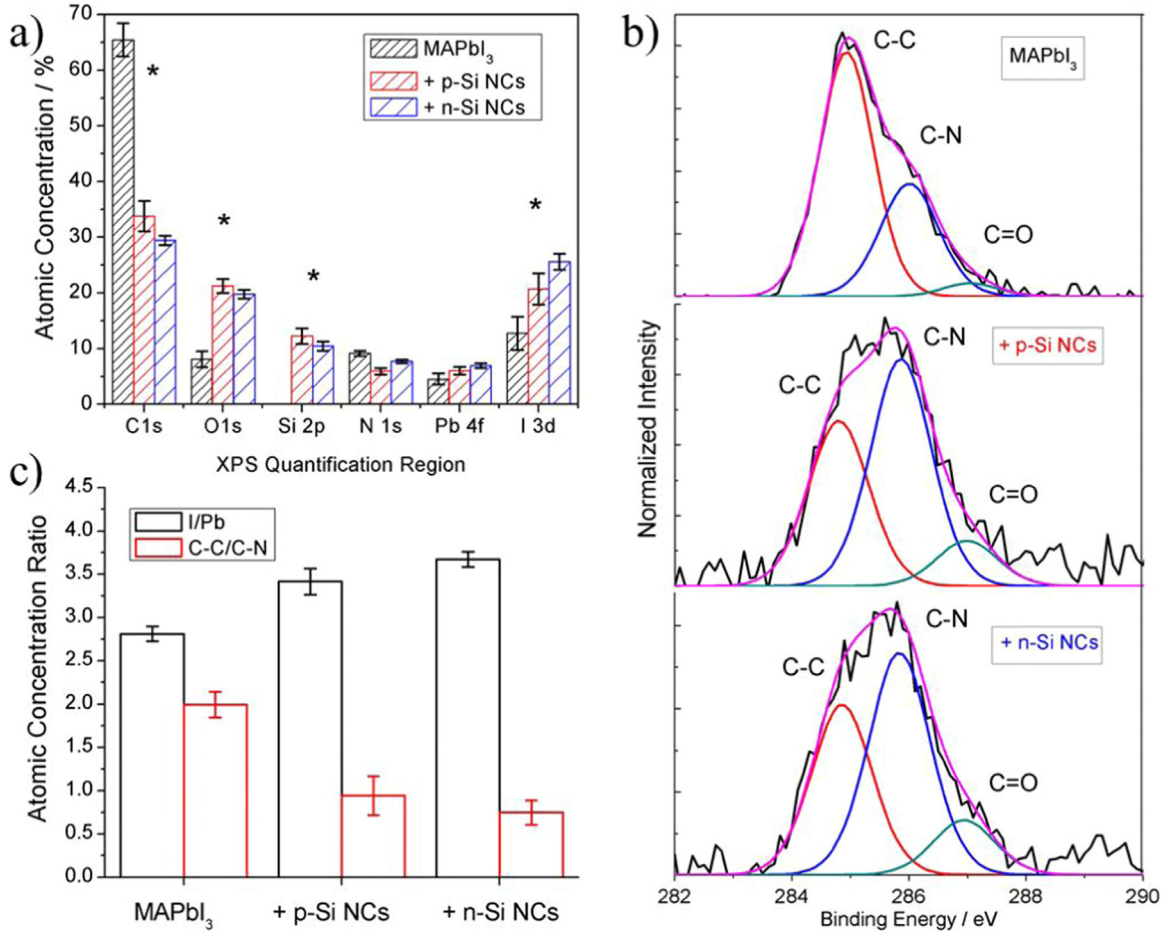

Fig. 1. a) Atomic concentrations for $MAPbI_3$, $MAPbI_3$ + p-Si NCs and $MAPbI_3$ + n-Si NCs films determined from XPS measurements with b) C 1s region scans and c) changes in I/Pb and C/C-N atomic concentrations.

made of $MAPbI_3$ + Si NCs (p- and n-type) and compare them with $MAPbI_3$-only films. X-ray photoelectron spectroscopy was used to determine the chemical composition of the films which were spray deposited on glass substrates. Specific core level scans were performed for C *1s*, O *1s*, Si *2p*, N *1s*, Pb *4f* and I *3d* regions and fitted using Gaussian line shapes after linear background subtraction. Fig. 4a shows the atomic concentration for each core level region which was determined from the integrated area under their peaks and plotted for $MAPbI_3$, $MAPbI_3$ + p-Si NCs and $MAPbI_3$ + n-Si NCs. There are three noticeable changes in the atomic concentrations as a consequence of adding doped Si NCs to the sprayed $MAPbI_3$ solution; these are highlighted with an '*' in Fig. 1a and correspond to C *1s* (far left), O *1s* (left), Si *2p* (centre) and I *3d* (far right). Firstly, as expected, the atomic concentration of Si *2p* increases for both $MAPbI_3$ films after the addition of p- and n-Si NCs. Secondly, the contribution of the C *1s* core level, typically made up of surface adsorbed hydrocarbon bonding arrangements, drops considerably after adding both p- and n-Si NCs (far left Fig. 1a). The O *1s* component almost doubles in concentration after adding the Si NCs and is expected to be due to surface oxidation of the NCs. Finally the concentration of iodide relative to the lead component of the perovskite increases (far right Fig. 1a).

The C *1s* spectra shown in Fig. 1b can be de-convoluted into 3 peaks at 284.8 eV, 286 eV and 287 eV that are assigned to sp^2 carbon (C-C) from surface adsorbed species, carbon bonded with nitrogen (C-N) that is ascribed to the perovskite organic core and carbon singly bonded with oxygen (C-O), respectively [25,26]. The addition of doped Si NCs in $MAPbI_3$ was observed to lower significantly carbon atomic concentration and deconvolution of the C *1s* spectra shows clearly that this is exclusively due to reduction of surface adsorbed C-C bonds relative to C–N bonding. Fig. 1c highlights changes in I/Pb atomic mass concentrations where I:Pb atomic mass ratios were calculated to be 2.81 for $MAPbI_3$, 3.41 for $MAPbI_3$ + p-Si NCs and 3.67 for $MAPbI_3$ + n-Si NCs (Fig. 1c). Typically a 3:1 at. concentration ratio for I:Pb is expected in the stoichiometric perovskite crystal but slightly lower values are characteristic for samples prepared in atmospheric conditions, due to the rapid degradation pathways in ambient air. For $MAPbI_3$ films that have been sprayed from a solution with Si NCs included, the I:Pb atomic concentration ratio well exceeds the predicted values. At the same time the ratio for C-C/C-N atomic concentrations of composite films is lower due to a more iodide concentrated surface (Fig. 1c).

Fig. 2 compares core level scans for a) Si *2p*, b) O *1s* and c) N *1s* for $MAPbI_3$ and $MAPbI_3$ with doped Si NCs. Core level spectra for Si *2p* in the $MAPbI_3$ only film has been included to confirm the non-existence of silicon (Fig. 1a). The p- and n- Si NCs integrated in the $MAPbI_3$ film show a metallic Si^0 peak located around 99.7 eV with oxide components Si^{1+}, Si^{2+}, Si^{3+} and Si^{4+} located at binding energies shifted by 0.95 eV, 1.57 eV, 2.56 eV and 3.82 eV respectively, relative to the Si^0 position [27]. It is evident that there has been some oxidation to both p- and n-Si NCs during the deposition process that would have been assisted by the $MAPbI_3$ annealing process. The O *1s* spectrum for $MAPbI_3$ film (Fig. 2b) show expected peaks at 532 eV and 533.8 eV that can be assigned to oxygen doubly bonded with carbon (O=C) and oxygen doubly bonded with a carboxyl (O=C-O), both due to adsorbed atmospheric hydrocarbons [28]. The peak at lower binding energy 530.5 eV (O′) is due to intercalated OH^-/O^{2-}, [28,29] signifying early chemical degradation of crystal structure in agreement with the I:Pb atomic mass

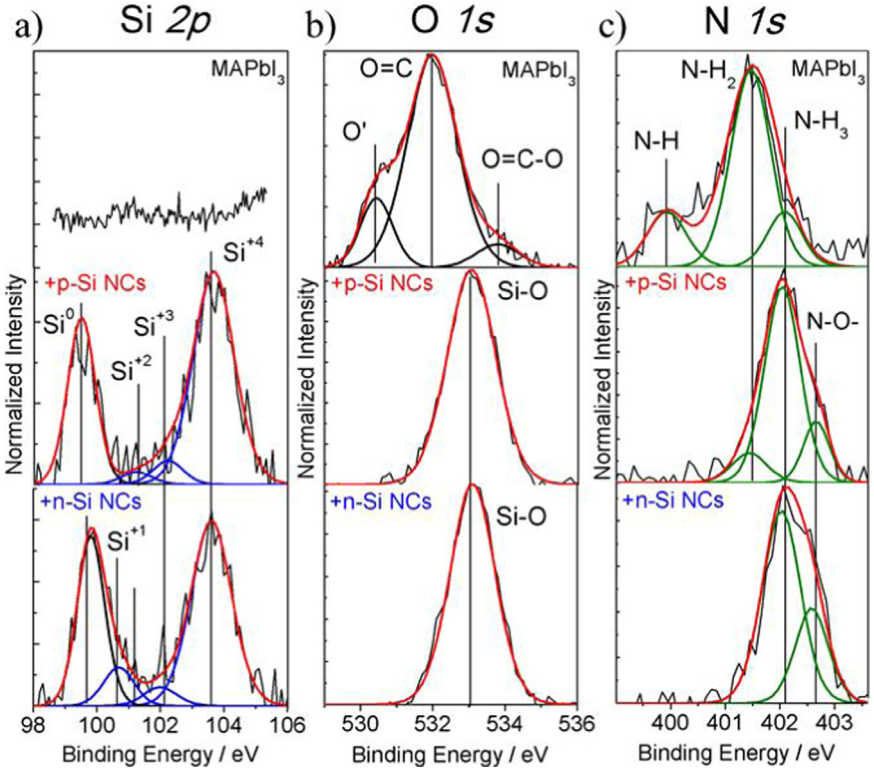

Fig. 2. X-ray photoelectron spectroscopy core level scans a) Si *2p* b) O *1s* and c) N *1s* for spray deposited $MAPbI_3$, $MAPbI_3$+ p-Si NCs and $MAPbI_3$+ n-Si NCs.

ratio of below 3 that was determined. The O *1s* for $MAPbI_3$+ p-Si NCs and $MAPbI_3$+ n-Si NCs is fitted with only a single peak located at 533.1 eV and is assigned to Si-O bonding from SiO_2 [30].

Fig. 2c shows the N *1s* spectrum for $MAPbI_3$ and shows a distinct peak at low binding energy with a more intense peak and shoulder peak shifted to higher energies. The low binding energy peak at 399.7 eV is associated with nitrogen singly bonded to carbon (-N-H) with two peaks at 401.1 eV and 401.9 eV corresponding to N-H_2 and N-H_3 singly bonded to carbon, respectively [31,32]. The weak hydrogen bonds in the protonated MA^+ ion ($CH_3NH_3^+$) is typically the source of chemical decomposition in $MAPbI_3$ and the ratio of NH_2 bonds to NH_3 is confirmation that some degradation of organic core has occurred. The N *1s* spectra after mixing p- and n-Si NCs in the $MAPbI_3$ film where the intensity of peak assigned to NH_3 bonding has increased relative to deprotonated NH_2 component. The addition of a small shoulder peak at binding energy 402.5 eV is traditionally credited to nitrogen atoms bonded to oxygen atoms (N-O), [33,34] proposing that some bonding of perovskite's organic core and Si NCs may be present through an intermediate oxide bond (N-O-Si). Comparison between spectra relating to Pb *4f* and I *3d* regions (not shown) showed no noticeable broadening of signal or shifts in binding energy, suggesting that Pb-I network does not interact chemically with the p- and n-Si NCs.

Fig. 3 shows XPS chemical analysis that has been carried out up to 14 days for both $MAPbI_3$ only and $MAPbI_3$ with Si NCs films where only $MAPbI_3$+ p-Si NCs are shown for simplicity; this highlights the changes in atomic concentration due to aging in atmosphere. The chemical decomposition of $MAPbI_3$ in ambient conditions is well understood and studied. With atomistic simulations and experimental data stating that deprotonation of the MA cation to form CH_3NH_2 is the initial first step as a consequence of intercalated moisture or oxygen species [35]. Further breakdown of the perovskite results in evaporation of NH_2 and HI components which is evident from the large decrease in both C *1s* and N *1s* after 7 days (Fig. 3a), due to the loss of C–N bonding. A small increase is observed for O *1s* which is due to the increase in weakly adsorbed OH^- and O^{2-} ions associated with the peak at 530.6 eV found in the O *1s* spectrum (Fig. 3b) [28,29]. Both Pb *4f* and I *3d* concentrations increase over time and is almost certainly due to the surface loss of the MA and HI species, leaving PbI_2. Examination of the change in I:Pb atomic concentration ratio over the 14 day period shows a decrease from 2.8:1 to 2:1 that is associated with PbI_2 formation (see Supporting information).

The degradation pathway for $MAPbI_3$+ p-Si NCs in atmosphere follows similar trends in comparison with C *1s* and N *1s* decreasing, however it is obvious that the gradient has reduced (Fig. 3b). The Si *2p* atomic concentration is initially above 10% and increases slightly over time, likely again due to evaporation of MA and HI species and making Si NCs more concentrated at the films surface. Most noticeably is the large increase in O *1s* concentration that is due to continued oxidation of the p-Si NCs at the surface of the composite film; in addition the reduction of the I:Pb concentration ratio is slowed down that remains close to 3:1 after 7 days and drops to around 2.6:1 after 14 days (see Supporting information). The slowed chemical decomposition of $MAPbI_3$ is attributed directly to the introduction of p-Si NCs throughout the film and their affinity for absorbing oxidizing species.

Fig. 3c depicts and summarizes the chemical changes at the surface of the perovskite-only films and that of the composite films. We should highlight that XPS can only probe the state of the surface of the films; therefore this analysis relates to the top 5–10 nm (XPS penetration depth) of the films and that we should expect the underlying bulk film to be less affected by ageing. Analysis of the $MAPbI_3$+ p- and n-Si NCs surface by XPS showed a significant decrease in C *1s* concentration and increase in the relative ratio of C–N to C–C bonds, signifying a more stoichiometric surface. Furthermore, underlining the reduced surface decomposition was the extremely high I:Pb atomic concentrations for $MAPbI_3$+ p- and n-Si NC films, that well exceed that expected for $MAPbI_3$ films produced in atmosphere. Extra iodide in films has previously been explained as being trapped in the form of triiodide (I_3^-) or $[PbI_6]^{4-}$ ions [36]. The degradation mechanism for $MAPbI_3$ in atmosphere has been covered in detail and is initiated with the deprotonation of NH_3 bond in the perovskites organic core [37]. The N *1s*

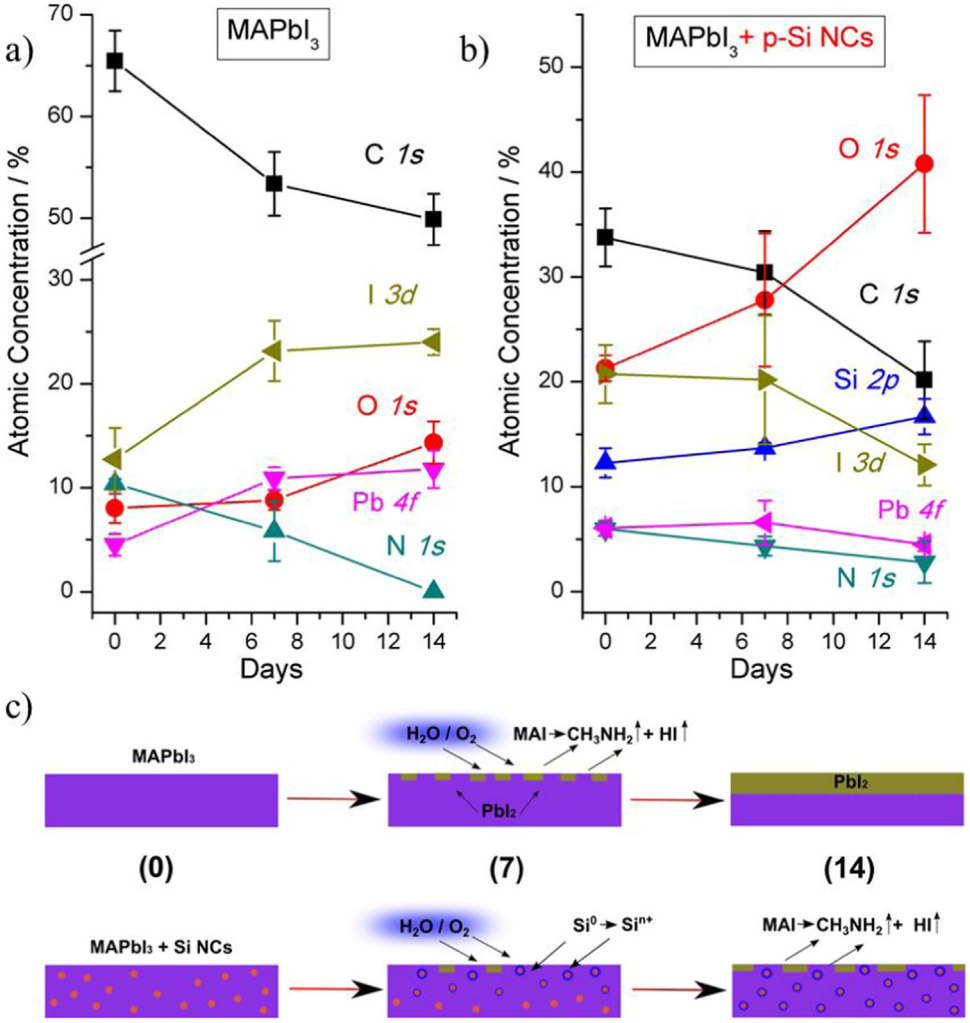

Fig. 3. Atomic concentration determined by XPS over time in atmosphere for a) $MAPbI_3$ films b) $MAPbI_3$+ p-Si NC films. c) schematic to show the typical $MAPbI_3$ surface degradation pathway (top) and the reduced degradation as a consequence of p- and n-Si NC inclusion (bottom).

spectrum for $MAPbI_3$ films after addition of p- and n-Si NCs increased NH_3 bonds relative to NH_2, in contrast with $MAPbI_3$ only films that were made up primarily of NH_2 and NH_x bonding arrangements.

An additional peak in the N *1s* region at binding energy 402.5 eV was assigned to nitrogen atoms bonded to oxygen (N-O) which suggests that Si NCs may bond with perovskite's organic core through intermediate oxide bonds (N-O-Si). Si NCs that are forced to $MAPbI_3$ grain boundaries or defects in lattice sites may act as passivating or binding agents through these oxide bridging bonds, further limiting the diffusion of moisture and other detrimental species. The increased stability of spray deposited $MAPbI_3$+ p- and n-Si NC films in comparison with $MAPbI_3$ only can be accredited to its interaction with oxidized Si NCs, shielding the highly volatile MA cation and maintaining the inorganic PbI framework.

3.2. Type-I alignment and electronic band diagram for $MAPbI_3$ and p-/n-Si NCs

The type-I junction proposed in this work implements two semiconductors within the active layer of the cell architecture where each individual material will be optimized to serve a single function either to absorb photons and generate carriers or to transport carriers to contacts. Fig. 4 shows a schematic of the operation of such a device where the two semiconductors show type-I or nested alignment within the active layer. One semiconductor will make up the bulk of the layer (Fig. 4, transporter) and exhibit enhanced transport properties whereas the other semiconductor (Fig. 4, absorber) will generate carriers. In this unique device structure, each semiconductor can be individually tailored to suit its function and in particular the absorber material is freed from the demanding challenge of meeting transport requirements. In Fig. 4 an example of such device is presented along with an electron transport material (ETL), hole transport layer (HTL), indium tin oxide (ITO) patterned glass and top contact.

For a type-I junction, charge transfer can occur through a number of mechanisms. Firstly electronic coupling (Fig. 4, left), where excitons/carriers generated in the wider bandgap absorber are transferred to the adjacent smaller bandgap conduction and valence bands; carrier dissociation/transport then can occur due to the electric field present within the transporter. A second mechanism for charge transfer can occur by optical coupling (Fig. 4, right) with the absorber essentially acting as a down converter for high energy photons, re-emitting at lower energy closer to the bandgap of the transporter. In this mechanism it is therefore important to match the peak photoluminescence (PL) wavelength with the bandgap energy of the transporter. Compared to the use of down-converter layers on top of the active layer, [38–40] this approach has the added advantage that embedded absorbers are surrounded by the active layer and therefore re-absorption is maximized. Of course, at some degree, electronic- and optical-coupling can co-exist in the same architecture so that both phenomena can take place and losses are minimized.

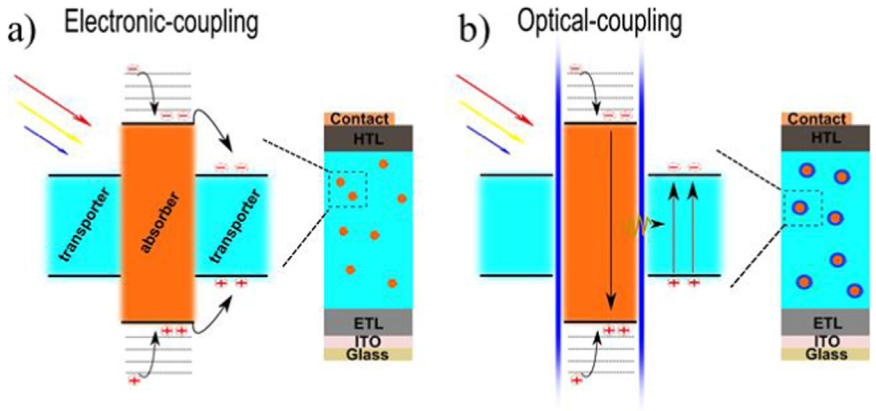

Fig. 4. Example of device architecture implementing novel type-I alignment with charge transfer occurring between the two semiconductors through either a) electronic coupling or b) optical coupling.

Here we have used our Si NCs/$MAPbI_3$ composite film for the active layer, where the Si NCs represents the absorber and the perovskite the transporter. In this specific case where perovskites are used as transporter, strong absorption takes place also in this component. In order to verify the possibility of forming a type-I junction we have carried out measurements to determine important parameters of the energy band diagram (band edges and Fermi level) of both Si NCs and $MAPbI_3$.

Fermi level measurements were performed using a Kelvin probe system that measures the contact potential difference of the material relative to a known work function reference, gold (− 5.1 eV) in this case. Fig. 5a shows the Fermi level measurements for $MAPbI_3$ film. Additionally, Fermi level measurements have been taken for p- and n-Si NCs that were synthesized by electrochemical etching, prepared and sonicated in DMF and sprayed onto bulk wafers of the corresponding doping (Fig. 5b-c). Fermi levels for p- and n-Si NCs compared with the corresponding doped bulk silicon substrate highlights the net energy shift due to quantum confinement. The Fermi levels for $MAPbI_3$, n-Si NCs and p-Si NCs lie around − 5.2 eV, − 4.4 eV (vs. − 4.29 eV for the bulk) and − 4.7 eV (vs. − 4.44 eV for the bulk) respectively and are in good agreement with values found in the literature [22].

Fig. 5d displays XPS low binding energy scans that can give insight into valence electrons and the density of states in relation to the Fermi level (E_F). Extrapolating the onset of the XPS signal enables the calculation of the valence band maximum (VBM) energy relative to our experimentally determined Fermi level. Clearly highlighted in the figure, the onset energy for $MAPbI_3$ is found at 0.6 eV and represents the I *5p* non-bonding state with a right shoulder peak around 4 eV that can be assigned to the anti-bonding hybrid state of Pb *6s* and I *5p* [41,42]. For p- and n-type Si NCs, the low signal has been increased by a factor of 4 to allow for comparison and shows a signal onset at 0.65 eV and 0.95 eV

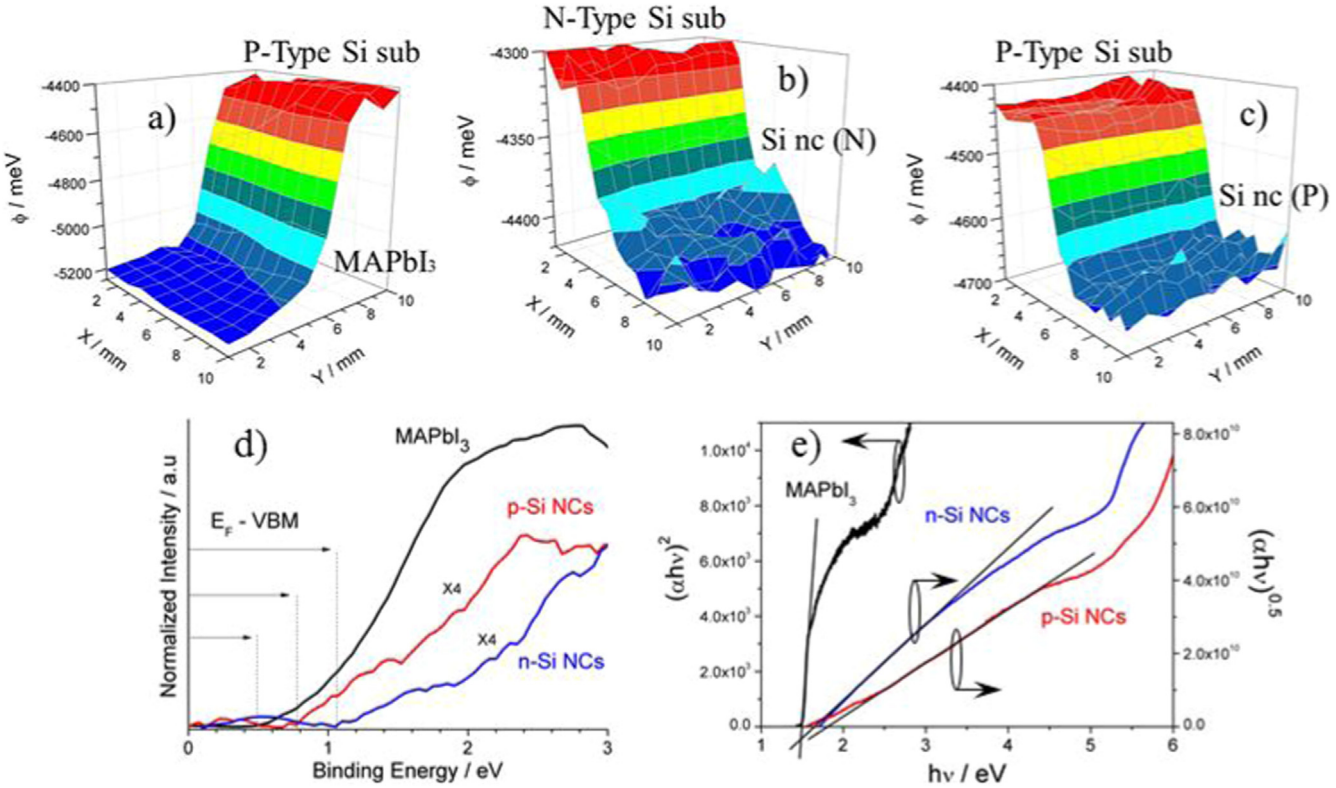

Fig. 5. Kelvin probe measurements to determine Fermi level of a) $MAPbI_3$, b) n-type Si NCs and c) p-type Si NCs. d) XPS low binding energy scans where the onset of the signal relates to the energy separation E_F – VBM and e) Tauc plots to calculate the bandgap energy for $MAPbI_3$ and p- and n-type Si NCs.

Table 1
Experimentally determined energy levels for $MAPbI_3$, p- and n-Si NCs including energy levels after Fermi equalization for $MAPbI_3$ + p-Si NCs and $MAPbI_3$ + n-Si NCs. All values in eV.

	Φ	Φ - VBM	VBM	E_g	CBM
MAPbI3	− 5.20	0.60	− 5.80	1.50	− 4.30
p-Si NCs	− 4.70	0.66	− 5.36	1.90	− 3.46
n-Si NCs	− 4.40	0.95	− 5.35	1.85	− 3.50
Oxidized p-Si NCs	− 5.42	0.65	− 6.07	2.18	− 3.89

respectively that is generated from Si *3p* electrons.

Fig. 5e presents Tauc plots for a $MAPbI_3$ film along with p- and n-type Si NCs. Absorption coefficients were determined by taking transmission measurements of thin films inside and outside of an integrated sphere in order to account for scattering and reflectance (see Supporting information). For the direct bandgap of $MAPbI_3$, the square of the absorption coefficient is linearly dependent on $h\nu$ at photon energies greater than the bandgap, which in this case is found to be 1.5 eV. Bulk Si has an indirect bandgap of 1.1 eV that widens due to the quantum confinement; in NCs, the bandgap is obtained from the linear dependence of the square root of the absorption coefficient on photon energies below the indirect bandgap [43]. Fitting the most linear section of the spectra for p- and n-type Si NCs, indirect bandgap values of 1.9 eV and 1.85 eV are estimated.

Table 1 summarizes the experimentally determined energy band levels for p-Si NCs, n-Si NCs and $MAPbI_3$; the conduction band minimum (CBM) was determined by adding the bandgap (E_g) to the measured VBM. On this basis and after Fermi level equilibration, Si NCs appears to form a type-I junction with the $MAPbI_3$ film (Figs. 7a and 7b). However, as we discussed earlier and demonstrated through XPS analysis (Fig. 2a), Si NCs undergo partial surface oxidation during the fabrication process of the composite. Because Si NCs surface oxidation may impact on the Si NCs energy levels, it is important to evaluate the band energy diagram of the Si NCs once these are integrated in the $MAPbI_3$ films. For simplicity, here below we will focus on p-type Si NCs again with the expectation that n-type Si NCs will follow a similar trend. Fermi levels and optical bandgap values however cannot be measured directly when the Si NCs are within the perovskite film. Therefore, in order to estimate these values, we have carried out measurements (as in Fig. 5, see Supporting information) of Si NCs with a different degree of oxidation.

The results are reported in Fig. 6 where the Fermi levels, VBM (determined from XPS and Fermi level measurements) and CBM (determined from the VBM and bandgap measurements) are reported vs. the oxidation degree expressed in terms of the ratio between the XPS Si^0 and Si^{4+} peaks. In Fig. 6 we also indicate the oxidation degree of the Si NCs embedded in the perovskite (dashed vertical line) as per our XPS measurements above (Fig. 2a). By interpolation of the trends, we can therefore estimate the energy band diagram for the surface-oxidized Si NCs when integrated in the $MAPbI_3$ films (stars in Fig. 6): − 6.07 eV for the VBM, − 5.42 eV for the Fermi level and 3.89 eV for the CBM (see also Table 1, oxidized p-Si NCs).

This analysis reveals a few very important points. Type-I alignment is confirmed for both as-prepared Si NCs as well as Si NCs that have undergone oxidation due to the composite fabrication process (Fig. 7c, which depict the equilibrated band diagram on the basis of the values in Table 1). Furthermore we can observe from Fig. 6 that for all different degrees of oxidation considered here, type-I alignment would be preserved between oxidized Si NCs and $MAPbI_3$. Although at some point, for extended oxidation, type-I alignment would disappear, we should note that Si NCs oxidation is halted because of limited diffusion due to geometrical constraints [44,45]. A degree of oxidation actually benefits type-I alignment compared to as-prepared Si NCs as the Fermi levels of oxidized Si NCs and $MAPbI_3$ approach the same value. Furthermore a thin oxide shell can be easily tunnelled through by carriers, decreases Si NCs surface defects and increases the photoluminescence quantum yield, [46] which are all phenomena that contribute to reduce carrier losses. As the composite films are exposed to the environment, we expect Si NCs to have different degree of oxidation, higher at the top of the film and less oxidized in the bulk of the composite film. However on the basis of our analysis, type-I alignment is preserved in all cases.

Based on the finding of Fig. 7, the wider bandgap of p- and n-Si NCs would act as the absorber generating carriers before transferring either electronically and/or optically to the bulk $MAPbI_3$ film. While general solar cell devices are based on type-II junctions, we believe that the introduction of a type-I heterojunction can bring greater benefits to overcome intrinsic transport limitation of QD-based solar cells. Type-I alignment also ensures that carriers that do recombine radiatively and would be lost in a standard type-II junction, are effectively re-generated within the transporter. Down shifting may be also important for future, long lasting and stable perovskite solar cells since high energy photons can cause internal stress and strain due the low thermal conductivity in $MAPbI_3$ films [47]. Since $MAPbI_3$ bandgap is relatively small (1.5 eV), a large part of the solar radiation is converted into heat which if not dissipated can result in stresses that lead to large decreases in efficiencies. The increased absorption coefficient in Si NCs coupled with their strong PL at energies close to the perovskites bandgap make them ideal for down conversion (see Supporting information) [48,49]. At the same time, high energy photons absorbed by Si NCs could otherwise generate multiple excitons in Si NCs that would be electronically or optically transferred to $MAPbI_3$, increasing the quantum efficiency of devices [17,50]. Since perovskite solar devices have a maximum achievable efficiency of around 31% according to the Shockley-Queisser limit, the inclusion of quantum confined NCs and their unique properties could create interesting 3rd generation solar architectures to overcome this limit.

3.3. Carrier extraction in photovoltaic test structures

In order to evaluate the ability of carrier extraction in the composite films, current-voltage measurements were performed for test devices with $MAPbI_3$, $MAPbI_3$ + p-Si NCs and $MAPbI_3$ + n-Si NCs and measured under continued light soaking from 0 to 8 min. Device test structure layout includes ITO patterned glass with compact TiO_2 layer and TiO_2 meso-porous layer sprayed followed by deposition of main absorber ($MAPbI_3$) and sputtered gold contacts (Fig. 8a). Since no hole transport material (HTM) was used the FF values were expected to remain low compared to highly efficient $MAPbI_3$ devices. The FF could be improved significantly by the introduction of HTM, where Spiro-OMETAD particularly in perovskite solar cells has seen efficiencies increase considerably [1,2]. However, Spiro-OMeTAD was not used to eliminate an additional variable in the time-dependent analysis due to Spiro-OMeTAD own degradation process. We should stress that the aim of these test devices was to understand the implementation and carrier extraction capabilities of our type-I composite films and there was no intention to provide record efficiencies for pure perovskite devices.

Fig. 8b-d shows the current density-voltage (JV) measurements of the best devices incorporating $MAPbI_3$, $MAPbI_3$ + p-Si NC and $MAPbI_3$ + n-Si NC films. Devices were illuminated from 0 to 8 min in order to monitor their performance over time and after a short stabilization period. The device that included $MAPbI_3$ only showed short-circuit current density around 10 mA cm^{-2} and 0.8 V at 0 min illumination before continued light soaking up to 8 min decreased the performance by ~ 50% (Fig. 8b). The introduction of p- and n-Si NCs (Figs. 8c and 8d) within the $MAPbI_3$ film increased short-circuit current density in devices to 16 mA cm^{-2} and 12.5 mA cm^{-2}, respectively. Furthermore, photovoltaic performance increased over the short illumination period for devices including p- and n-Si NCs, reaching ~ 20 mA cm^{-2}. Analysis of photovoltaic parameters over a number of devices demonstrated the repeatability of the results and trends. The corresponding *Voc*, *Jsc*, FF and efficiency parameters under light

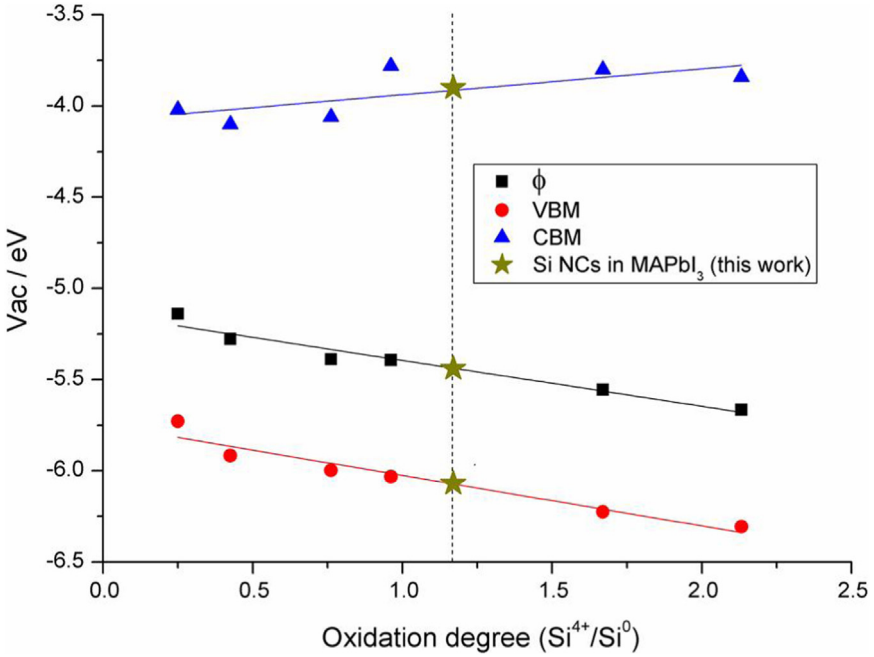

Fig. 6. Measured Fermi, VBM and CBM energy levels for p-Si NCs vs. p-Si NC oxidation degree expressed in terms of the ratio between XPS Si^0 and Si^{4+} peaks.

soaking conditions from 0 to 8 min for $MAPbI_3$ only devices, $MAPbI_3$ + p-Si NCs and $MAPbI_3$ + n-Si NCs are presented in the Supporting information.

Fig. 9a presents a summary of the device power conversion efficiency (PCE) of all devices at 0 min and after 8 min illumination. PCE of $MAPbI_3$ devices showed large instabilities over the short time period decreasing from a mean value of 2.64–0.87% (Fig. 9a). In comparison, $MAPbI_3$ composite devices that have included p- and n-Si NCs show substantial increases in average PCE from 2.44% to 4.28% and 1.48% to 4.15%, respectively. The incorporation of p- and n-Si NCs within the $MAPbI_3$ devices exhibits positive light soaking behaviour over the short time period in contrast with $MAPbI_3$ only devices. As previously discussed the I:Pb atomic mass ratio is increased for $MAPbI_3$ films with p- and n-Si NCs, beyond values typically associated with stoichiometric perovskite (Fig. 1c), which implies additional iodide is trapped within the films and allows for slower surface chemistry and degradation.

The comparison in PV performance and specifically the light response over time is an important factor in determining the practicability of devices in a real environment. Examining the trends in PV parameters over the illumination period (0–8 min) shows that $MAPbI_3$ only device drops off in performance. Due to a number of intrinsic phenomena of the perovskites complex structure, JV measurements are typically presented after stabilization period within a short time scale (120 s) [51,52]. Typically, perovskite based devices that include pristine $MAPbI_3$ films, fabricated in an inert atmosphere, show rapid increases in performance over this short time period. The reason for the improvement in PV performance is attributed to a number of effects such as polarization, ion migration or trapping/de-trapping of charge carriers that can all act simultaneously [53–55]. $MAPbI_3$ films in this study are fabricated in ambient conditions and consequently show surface degradation that does not resemble the stoichiometric crystal structure. The diffusing species and contaminants from the atmosphere immediately cause the I:Pb atomic concentration to lower to 2.8:1 which affects the perovskites JV performance over the illumination

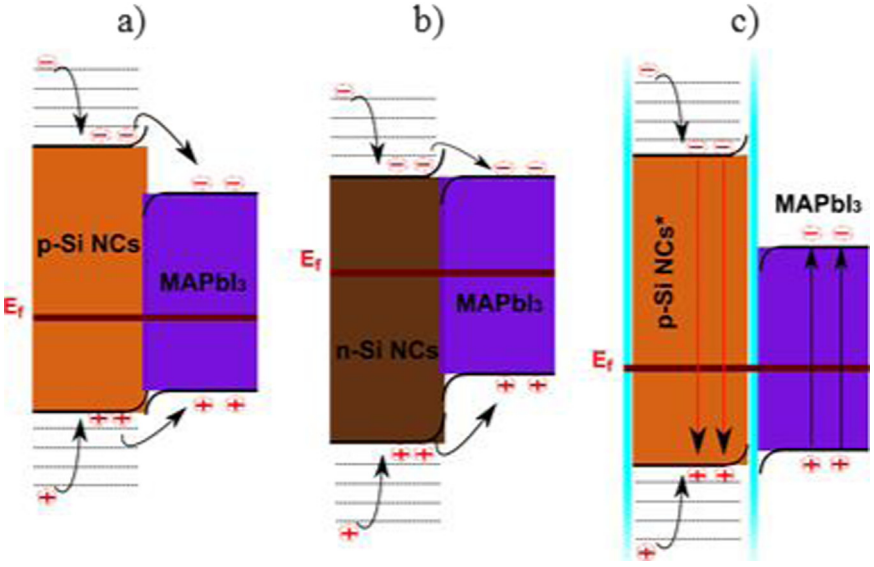

Fig. 7. Equilibrated energy band diagram of a) $MAPbI_3$ + p-Si NCs b) $MAPbI_3$ + n-Si NCs and c) $MAPbI_3$ + surface oxidized p-Si NCs*.

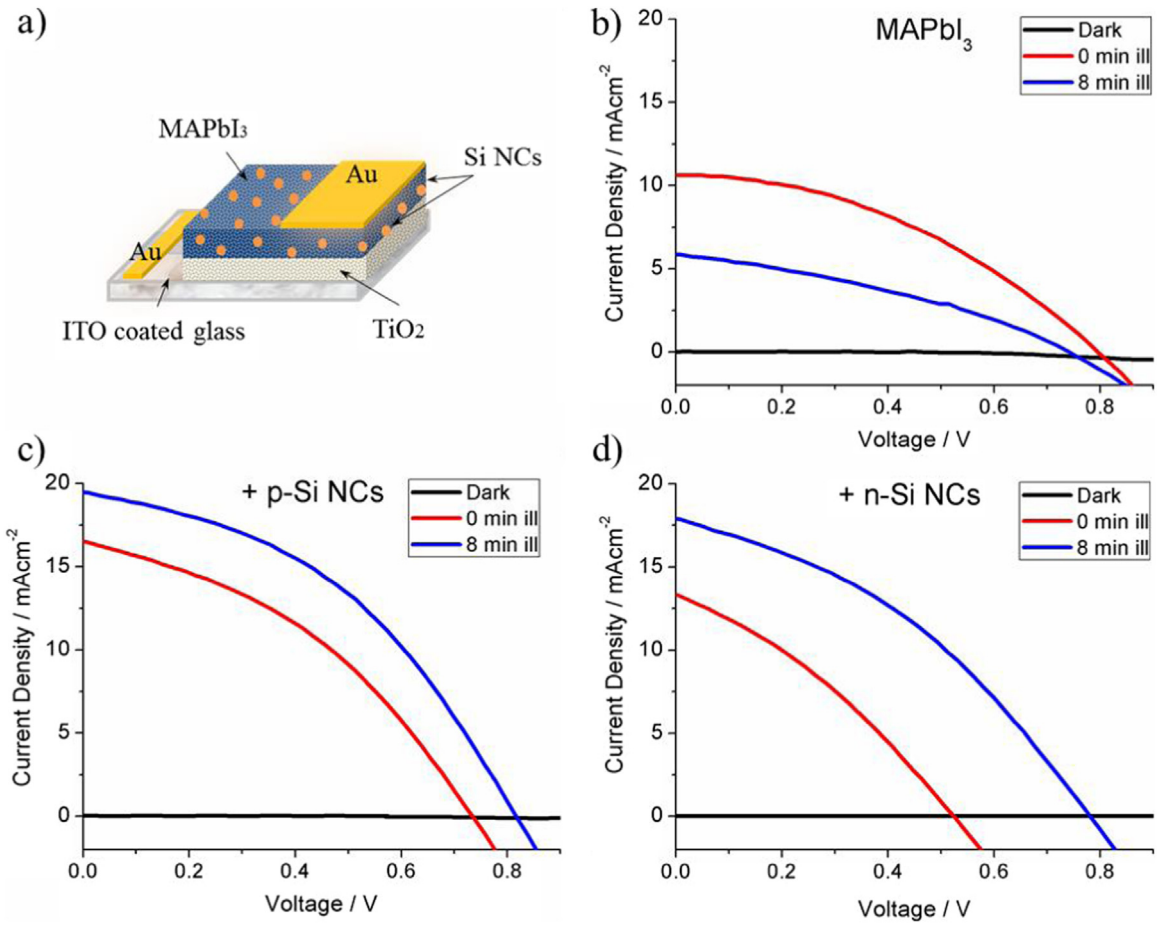

Fig. 8. a) $MAPbI_3$ based device structure b) current-voltage measurements in dark, at 0 min illumination and after 8 min illumination for $MAPbI_3$ only devices c) $MAPbI_3$ + p-Si NC and d) $MAPbI_3$ + n-Si NC solar devices.

period (0–8 min), where a negative trend is observed (Fig. 9a). This reduction under illumination has previously been attributed to the $MAPbI_3$ surface degradation which quenches carrier collection at the back electrode [24].

The incorporation of p- and n-Si NCs within the $MAPbI_3$ films improved *Jsc* at 0 min illumination however the *Voc* suffers and reduces to values around 0.6 V (+ p-Si NCs) and 0.45 V (+ n-Si NCs). The losses in *Voc*, compared to $MAPbI_3$-only devices, originate from the alignment of $MAPbI_3$ with Si NCs where there is potential for low energy barriers at the interfaces and/or the introduction of alternative recombination pathways. Similarly, differences between devices with p-Si NCs and n-Si NCs have to be ascribed to a better type-I alignment for p-type Si NCs as shown in Fig. 7. It is important to note that these results demonstrate effective carrier extraction in devices with type-I alignment where the short-circuit current outperforms that of $MAPbI_3$-only films; also, continued illumination for $MAPbI_3$ + p- and n-Si NC devices has had positive effects on JV parameters before stabilizing at higher efficiencies (Fig. 9a). Through detailed surface analysis the role of Si NCs within the $MAPbI_3$ film is shown to be complimentary due to their hydrophilic nature and high water retention, [56] protecting the hygroscopic MA cation from diffusing moisture [57].

3.4. Device performance over days

Fig. 9b shows the PCE for $MAPbI_3$ only devices, along with $MAPbI_3$ + p-Si NC and $MAPbI_3$ + n-Si NC devices at 0 days and 14 days in atmosphere. XPS chemical analysis (Fig. 3c) over time showed typical degradation pathways that are expected in $MAPbI_3$ films, resulting in the formation of PbI_2 at the surface through the evaporation of MAI components. Examining the PCE of the $MAPbI_3$-only devices, a 40% decrease in efficiency after 4 days is observed (see Supporting information) and continued aging in atmosphere results in a substantial loss of 80% after a total of 14 days (Fig. 9b).

Counter to this, type-I devices with either p- and n-Si NCs within $MAPbI_3$ films slows this chemical degradation (Fig. 3c). Moisture within the film results in the oxidation of p- and n-Si NCs at the surface of the film rather than the partial dissolution of perovskite's core that inevitably leads to the breakdown of perovskite lattice. This is evident from XPS measurements over time in atmosphere where Si *2p* and O *1s* atomic concentrations increased due to the absorption of moisture and oxygen species (Fig. 3b). As a consequence, the reduction of C *1s* and N *1s* atomic concentrations due to evaporating MAI component is slowed. As previously discussed, the reduced degradation is corroborated by the I:Pb atomic concentration where after 7 days the perovskite crystal is unaffected (3:1) and drops marginally (2.6:1) after 14 days. The enhanced stability of the composite films with Si NCs is directly linked to the more stable PCE of the type-I devices. After 4 days aging the $MAPbI_3$ + p-Si NC and $MAPbI_3$ + n-Si NC devices reduce by 10% and 20%, respectively (see Supporting information) and further aging in atmosphere sees devices only drop by a maximum of 30% (Fig. 9b).

These composite films show interesting features that encourage more investigation to develop and understand Si NC-$MAPbI_3$ systems and in general type-I heterojunctions with QDs. Here we have demonstrated that carrier extraction in a perovskite-Si NCs type-I film is possible. In general, the implementation of QDs in devices based on a type-I alignment appear to be a realistic avenue to overcome some of the limitations in QD-based solar cells. A number of improvements in device fabrication, particularly in the selection of the materials are

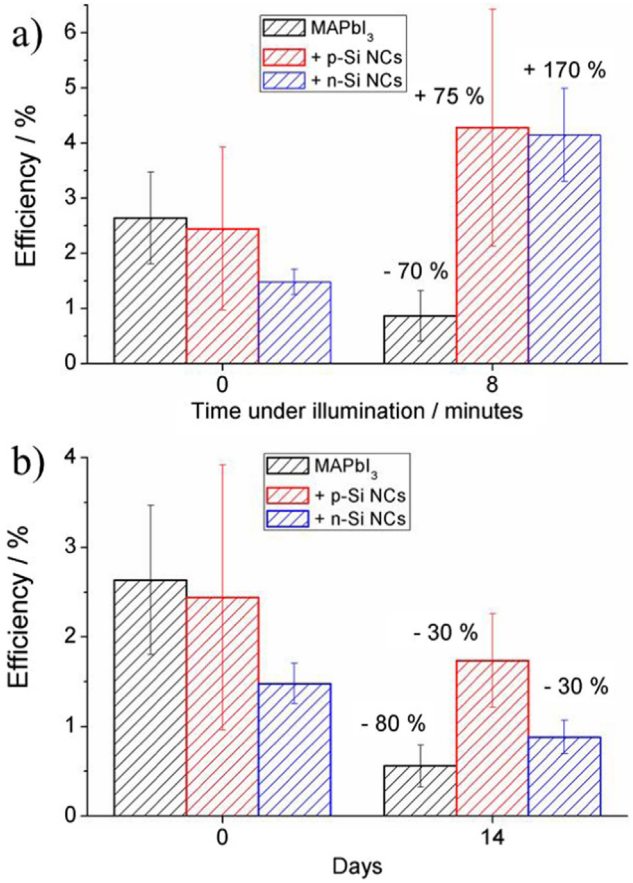

Fig. 9. a) PCE of $MAPbI_3$, $MAPbI_3$ + p-Si NC and $MAPbI_3$ + n-Si NC devices at 0 min and 8 min illumination b) PCE of devices at 0 day and after 14 days in atmosphere.

obvious advancements that could allow for efficient and longer lasting QD-based devices. Nevertheless, coupling quantum confined nanocrystals and their unique characteristics with large grained perovskites will lead to interesting architectures and exciting phenomena.

4. Conclusion

Owing to Si NCs strong absorption of high energy photons and PL close to the bandgap of $MAPbI_3$ perovskite, efforts were made to investigate the potential coupling of their unique opto-electronic properties in an atypical and novel type-I heterojunction. Using a number of complementing techniques the energy band diagrams for $MAPbI_3$ and p-/n-Si NCs were determined and potential alignment and charge transfer mechanisms discussed. This demonstrated type-I alignment and the possibility of effective carrier extraction. Detailed XPS also highlighted interesting features in $MAPbI_3$ surface chemistry as a consequence of mixing with both p- and n-Si NCs. The Si NCs due to their hydrophilic nature absorbed diffusing moisture and became oxidized which consequently slowed the chemical decomposition of $MAPbI_3$ perovskite. Composite $MAPbI_3$/Si NC films were incorporated into solar devices and showed improved PV performance and stability.

Overall the work suggest that a device architecture based on type-I alignment can offer great opportunities for QD-based solar cells in general. The specific implementation of QDs with perovskites also appears to present synergies that can be tuned to enhance both QD and perovskite key features. Si NCs in particular are well suited both in terms of the electronic structure as well as in light of the chemical analysis. In particular the formation of chemical bonds through an oxygen bridge is intriguing and exciting, which could provide unforeseen tunability. Future work will aim to quantify the contribution of Si NCs and their opto-electronic properties within the $MAPbI_3$ films as well as optimizing the concentration. Type-I alignment therefore opens up a large number of possible work directions for future third generation solar cells.

Acknowledgments

This research has been partially funded EPSRC (EP/K022237/1 and EP/M024938/1) and InvestNI (PoC-608). CR would also link to thank the Northern Ireland Department for Employment and Learning (DEL). This work was also partially supported by a NEDO Project (Japan).

Conflicts of interest

There are no conflicts of interest to declare.

Appendix A. Supporting information

Supplementary data associated with this article can be found in the online version at http://dx.doi.org/10.1016/j.nanoen.2018.05.036.

References

[1] J. Burschka, N. Pellet, S.-J. Moon, R. Humphry-Baker, P. Gao, M.K. Nazeeruddin, M. Grätzel, Nature 499 (2013) 316–320.
[2] M. Liu, M.B. Johnston, H.J. Snaith, Nature 501 (2013) 395–398.
[3] R. Fan, Y. Huang, L. Wang, L. Li, G. Zheng, H. Zhou, Adv. Energy Mater. (2016) 1600460.
[4] J.H. Heo, D.H. Song, H.J. Han, S.Y. Kim, J.H. Kim, D. Kim, H.W. Shin, T.K. Ahn, C. Wolf, T.-W. Lee, S.H. Im, Adv. Mater. 27 (2015) 3424–3430.
[5] A.A. Bakulin, O. Selig, H.J. Bakker, Y.L.A. Rezus, C. Müller, T. Glaser, R. Lovrincic, Z. Sun, Z. Chen, A. Walsh, J.M. Frost, T.L.C. Jansen, J. Phys. Chem. Lett. 6 (2015) 3663–3669.
[6] F. Polarization, N.H. Pbi, H. Kim, S.K. Kim, B.J. Kim, K. Shin, M.K. Gupta, H.S. Jung, S. Kim, N. Park, J. Phys. Chem. Lett. 6 (2015) 1729–1735.
[7] J. Haruyama, K. Sodeyama, L. Han, Y. Tateyama, J. Am. Chem. Soc. 137 (2015) 10048–10051.
[8] I. Deretzis, A. Alberti, G. Pellegrino, E. Smecca, F. Giannazzo, N. Sakai, T. Miyasaka, A. La Magna, Appl. Phys. Lett. 106 (2015) 131904.
[9] J.M. Frost, K.T. Butler, F. Brivio, C.H. Hendon, M. van Schilfgaarde, A. Walsh, Nano Lett. 14 (2014) 2584–2590.
[10] A. Alberti, I. Deretzis, G. Pellegrino, C. Bongiorno, E. Smecca, G. Mannino, F. Giannazzo, G.G. Condorelli, N. Sakai, T. Miyasaka, C. Spinella, A. La Magna, ChemPhysChem 16 (2015) 3064–3071.
[11] S.M. Haidary, E.P. Córcoles, N.K. Ali, J. Nanomater. 2012 (2012) 1–15.
[12] F. Maier-Flaig, J. Rinck, M. Stephan, T. Bocksrocker, M. Bruns, C. Kübel, A.K. Powell, G.A. Ozin, U. Lemmer, Nano Lett. 13 (2013) 475–480.
[13] C.-Y. Liu, U.R. Kortshagen, Nanoscale Res. Lett. 5 (2010) 1253–1256.
[14] C. de, M. Donegá, Chem. Soc. Rev. 40 (2011) 1512–1546.
[15] D. Kovalev, H. Heckler, G. Polisski, J. Diener, F. Koch, Opt. Mater. 17 (2001) 35–40.
[16] D. Das, A. Samanta, Phys. Chem. Chem. Phys. 17 (2015) 5063–5071.
[17] M.C. Beard, K.P. Knutsen, P. Yu, J.M. Luther, Q. Song, W.K. Metzger, R.J. Ellingson, A.J. Nozik, Nano Lett. 7 (2007) 2506–2512.
[18] Y. Cao, Z. Ge, X. Jiang, J. Xu, L. Xu, W. Li, L. Yu, K. Chen, Part. Part. Syst. Charact. 33 (2016) 38–43.
[19] S. Albrecht, M. Saliba, J.P. Correa Baena, F. Lang, L. Kegelmann, M. Mews, L. Steier, A. Abate, J. Rappich, L. Korte, R. Schlatmann, M.K. Nazeeruddin, A. Hagfeldt, M. Grätzel, B. Rech, Energy Environ. Sci. 9 (2016) 81–88.
[20] R.S. Sanchez, M.S. de la Fuente, I. Suarez, G. Munoz-Matutano, J.P. Martinez-Pastor, I. Mora-Sero, Sci. Adv. 2 (2016) (e1501104–e1501104).
[21] D. Mariotti, V. Švrček, J.W.J. Hamilton, M. Schmidt, M. Kondo, Adv. Funct. Mater. 22 (2012) 954–964.
[22] T. Velusamy, S. Mitra, M. Macias-Montero, V. Svrcek, D. Mariotti, ACS Appl. Mater. Interfaces 7 (2015) 28207–28214.
[23] V. Svrcek, in Optoelectronic Devices and Properties, InTech, 2011.
[24] C. Rocks, V. Svrcek, P. Maguire, D. Mariotti, J. Mater. Chem. C 5 (2017) 902–916.
[25] S. Barman, M. Sadhukhan, J. Mater. Chem. 22 (2012) 21832.
[26] A.L. Abdelhady, M.I. Saidaminov, B. Murali, V. Adinolfi, O. Voznyy, K. Katsiev, E. Alarousu, R. Comin, I. Dursun, L. Sinatra, E.H. Sargent, O.F. Mohammed, O.M. Bakr, J. Phys. Chem. Lett. 7 (2016) 295–301.
[27] M. Boström, B.W. Ninham, I. Brevik, C. Persson, D.F. Parsons, B.E. Sernelius, Appl. Phys. Lett. 100 (2012) 253104.
[28] G. Rajendra Kumar, A. Dennyson Savariraj, S.N. Karthick, S. Selvam, B. Balamuralitharan, H.-J. Kim, K.K. Viswanathan, M. Vijaykumar, K. Prabakar, Phys. Chem. Chem. Phys. 18 (2016) 7284–7292.
[29] W. Huang, J.S. Manser, P.V. Kamat, S. Ptasinska, Chem. Mater. 28 (2016) 303–311.
[30] T.V. Larina, L.S. Dovlitova, V.V. Kaichev, V.V. Malakhov, T.S. Glazneva,

E.A. Paukshtis, B.S. Bal'zhinimaev, RSC Adv. 5 (2015) 79898–79905.
[31] G.M. Fuge, C.J. Rennick, S.R.J. Pearce, P.W. May, M.N.R. Ashfold, Diam. Relat. Mater. 12 (2003) 1049–1054.
[32] R. Naphade, S. Nagane, G.S. Shanker, R. Fernandes, D. Kothari, Y. Zhou, N.P. Padture, S. Ogale, ACS Appl. Mater. Interfaces 8 (2016) 854–861.
[33] J.S. Park, J.M. Lee, S.K. Hwang, S.H. Lee, H.-J. Lee, B.R. Lee, H. Il Park, J.-S. Kim, S. Yoo, M.H. Song, S.O. Kim, J. Mater. Chem. 22 (2012) 12695.
[34] R. Scaffaro, L. Botta, G. Lo Re, R. Bertani, R. Milani, A. Sassi, J. Mater. Chem. 21 (2011) 3849.
[35] L. Zhang, P.H.-L. Sit, J. Phys. Chem. C 119 (2015) 22370–22378.
[36] L.A. Frolova, N.N. Dremova, P.A. Troshin, Chem. Commun. 51 (2015) 14917–14920.
[37] Y. Ren, I.W.H. Oswald, X. Wang, G.T. McCandless, J.Y. Chan, Cryst. Growth Des. 16 (2016) 2945–2951.
[38] S. Mitra, S. Cook, V. Švrček, R.A. Blackley, W. Zhou, J. Kovač, U. Cvelbar, D. Mariotti, J. Phys. Chem. C 117 (2013) 23198–23207.
[39] V. Svrcek, T. Yamanari, D. Mariotti, S. Mitra, T. Velusamy, K. Matsubara, Nanoscale 7 (2015) 11566–11574.
[40] V. Svrcek, T. Yamanari, D. Mariotti, S. Mitra, K. Matsubara, in 2014 IEEE Proceedings of the 40th Photovoltaic Specialist Conference (PVSC), IEEE, 2014, pp. 1556–1559.
[41] H. Xu, Y. Wu, J. Cui, C. Ni, F. Xu, J. Cai, F. Hong, Z. Fang, W. Wang, J. Zhu, L. Wang, R. Xu, F. Xu, Phys. Chem. Chem. Phys. 18 (2016) 18607–18613.
[42] Y. Yuan, R. Xu, H.-T. Xu, F. Hong, F. Xu, L.-J. Wang, Chin. Phys. B 24 (2015) 116302.
[43] M. Macias-Montero, S. Askari, S. Mitra, C. Rocks, C. Ni, V. Svrcek, P.A. Connor, P. Maguire, J.T.S. Irvine, D. Mariotti, Nanoscale 8 (2016) 6623–6628.
[44] U. Khalilov, G. Pourtois, A.C.T. van Duin, E.C. Neyts, Chem. Mater. 24 (2012) 2141–2147.
[45] M. Zacharias, 2006, 2006–2008.
[46] W.L. Wilson, P.F. Szajowski, L.E. Brus, Science (80-.) 262 (1993) 1242–1244.
[47] A. Pisoni, J. Jaćimović, O.S. Barišić, M. Spina, R. Gaál, L. Forró, E. Horváth, J. Phys. Chem. Lett. 5 (2014) 2488–2492.
[48] X. Wen, P. Zhang, T.A. Smith, R.J. Anthony, U.R. Kortshagen, P. Yu, Y. Feng, S. Shrestha, G. Coniber, S. Huang, Sci. Rep. 5 (2015) 12469.
[49] L. Pavesi, L. Dal Negro, C. Mazzoleni, G. Franzò, F. Priolo, Nature 408 (2000) 440–444.
[50] M.T. Trinh, R. Limpens, W.D.A.M. de Boer, J.M. Schins, L.D.A. Siebbeles, T. Gregorkiewicz, Nat. Photonics 6 (2012) 316–321.
[51] H.J. Snaith, A. Abate, J.M. Ball, G.E. Eperon, T. Leijtens, N.K. Noel, S.D. Stranks, J.T.-W. Wang, K. Wojciechowski, W. Zhang, J. Phys. Chem. Lett. 5 (2014) 1511–1515.
[52] S.D. Stranks, V.M. Burlakov, T. Leijtens, J.M. Ball, A. Goriely, H.J. Snaith, Phys. Rev. Appl. 2 (2014) 034007.
[53] S. Meloni, T. Moehl, W. Tress, M. Franckevičius, M. Saliba, Y.H. Lee, P. Gao, M.K. Nazeeruddin, S.M. Zakeeruddin, U. Rothlisberger, M. Graetzel, Nat. Commun. 7 (2016) 10334.
[54] Y. Yuan, J. Huang, Acc. Chem. Res. 49 (2016) 286–293.
[55] I. Levine, P.K. Nayak, J.T.-W. Wang, N. Sakai, S. Van Reenen, T.M. Brenner, S. Mukhopadhyay, H.J. Snaith, G. Hodes, D. Cahen, J. Phys. Chem. C 120 (2016) 16399–16411.
[56] Z. Chen, M. Qin, Energy Procedia 78 (2015) 201–206.
[57] S.R. Raga, M.-C. Jung, M.V. Lee, M.R. Leyden, Y. Kato, Y. Qi, Chem. Mater. 27 (2015) 1597–1603.